A second-order-in-time, explicit approach addressing the redundancy in the low-Mach, variable-density Navier-Stokes equations

Bryan W. Reuter^{a,*}, Todd A. Oliver^b, Robert D. Moser^{b,c}

^aSandia National Laboratories

^bCenter for Predictive Engineering and Computational Sciences,

Oden Institute for Computational Engineering and Sciences, The University of Texas-Austin

^cDepartment of Mechanical Engineering, The University of Texas-Austin

Abstract

A novel algorithm for explicit temporal discretization of the variable-density, low-Mach Navier-Stokes equations is presented here. Recognizing there is a redundancy between the mass conservation equation, the equation of state, and the transport equation(s) for the scalar(s) which characterize the thermochemical state, and that it destabilizes explicit methods, we demonstrate how to analytically eliminate the redundancy and propose an iterative scheme to solve the resulting transformed scalar equations. The method obtains second-order accuracy in time regardless of the number of iterations, so one can terminate this subproblem once stability is achieved. Hence, flows with larger density ratios can be simulated while still retaining the efficiency, low cost, and parallelizability of an explicit scheme. The temporal discretization algorithm is used within a pseudospectral direct numerical simulation which extends the method of Kim, Moin, and Moser for incompressible flow [17] to the variable-density, low-Mach setting, where we demonstrate stability for density ratios up to ~ 25.7 .

 $\label{lem:condition} \textit{Keywords:} \ \ \textit{Temporal discretization, Low-Mach-number, Variable-density Navier-Stokes, Iterative methods$

1. Introduction

Low-speed turbulent flows with significant density variations are common in engineering and nature, such as in turbulent combustion, nonreacting mixing problems, the atmosphere, and the oceans. In turbulent and other complex time-dependent flows, cost considerations drive a preference for explicit time discretization of the convection processes because, in such flows, the explicit stability limits on the time step are generally comparable to the limits imposed by accuracy requirements [24]. However, when the compressible Navier-Stokes equations are applied to low-Mach-number flows, acoustic wave propagation imposes much more severe stability limits on explicit time discretizations. For such flows, low-Mach-number variable density formulations (low-Mach) of the Navier-Stokes equations are good approximations to the fully compressible equations and eliminate the stability constraints imposed by acoustic wave propagation. Therefore, for simulation of complex or turbulent low-speed variable density flows, stable explicit time discretization of the low-Mach Navier-Stokes equations is needed, which is the subject of this paper.

In the low-Mach-number limit, the pressure fluctuations are decoupled from the density fluctuations. The pressure can then be decomposed into a uniform background, thermodynamic pressure and a mechanical pressure. The mechanical pressure fluctuates in space and time and acts to enforce mass conservation via a divergence constraint on the momentum as in incompressible flow. However, unlike constant-density incompressible flow, there is a time derivative term in the mass conservation equation, $\partial \rho/\partial t$, for variable-density flow which presents additional numerical challenges, particularly with large density variation. Two particular challenges are additional complexity in the treatment of the mechanical pressure and redundancy in the low-Mach-number Navier-Stokes equations which can lead to inconsistencies in the state and, as a consequence, instability.

^{*}Corresponding author

Email addresses: bwreute@sandia.gov (Bryan W. Reuter), oliver@oden.utexas.edu (Todd A. Oliver), rmoser@oden.utexas.edu (Robert D. Moser)

Despite these challenges and the computational cost of addressing them, it is often advantageous to employ the low-Mach formulation in low-speed flows instead of a conceptually simpler explicit treatment of the compressible formulation. This is because of the orders of magnitude smaller time step that is commonly needed for the compressible formulation due to the stability constraints imposed by acoustic wave propagation. In flow problems requiring grids with fine resolution in regions where the fluid velocity is small (e.g., near walls), the low-Mach formulation is advantageous even if, as is sometimes done, the acoustic wave speed is artificially reduced in the compressible formulation.

1.1. Treatment of the mechanical pressure in fractional step methods

Due to the similar role of the mechanical pressure, most numerical methods for solving the low-Mach equations are based on traditional incompressible fractional-step, projection methods [18, 27]. Fractional-step algorithms for incompressible flows solve for an intermediate velocity or momentum field $(u_i^* \text{ or } (\rho u_i)^*)$ by neglecting ("pressure-free" methods [6]) or lagging ("incremental" methods [13]) the pressure in the momentum equations and then projecting the result onto a divergence-free basis through the solution of a Poisson equation derived from the momentum equations. Since the momentum field is not divergence free in variable-density flows, standard incompressible projection methods must be modified. Within the class of fractional-step methods for the low-Mach equations, two formulations are commonly employed. One option is to take the divergence of the momentum equations, giving a constant-coefficient Poisson equation for the pressure correction δp , e.g.,

$$\Delta t \frac{\partial^2 \delta p}{\partial x_i \partial x_i} = \frac{\partial (\rho u_i)^*}{\partial x_i} - \frac{\partial (\rho u_i)^{n+1}}{\partial x_i}. \tag{1}$$

Here and throughout, we use Cartesian tensor notation and the Einstein summation convention. This is akin to the pressure Poisson equation in algorithms for incompressible flow. The divergence of the unknown momentum $(\rho u_i)^{n+1}$ is replaced with $-(\partial \rho/\partial t)^{n+1}$ by applying the mass conservation equation. A second option involves manipulating the advective form of the momentum equations to give a variable-coefficient Poisson equation, e.g.,

$$\Delta t \frac{\partial}{\partial x_i} \left(\frac{1}{\rho^{n+1}} \frac{\partial \delta p}{\partial x_i} \right) = \frac{\partial u_i^*}{\partial x_i} - \frac{\partial u_i^{n+1}}{\partial x_i}$$
 (2)

and employing the identity

$$\frac{\partial u_i}{\partial x_i} = -\frac{1}{\rho} \frac{D\rho}{Dt}$$

to replace the divergence of the unknown velocity u_i^{n+1} .

The first approach (equation (1)) has the advantage of being much easier to solve, but error in the evaluation of the density time derivative can lead to instability, especially when density ratios are larger than three [18, 29, 25]. To help alleviate this issue, predictor-corrector schemes or implicit formulations have shown some success [33, 26, 34, 16, 10]. Predictor-corrector methods are attractive in scenarios where only explicit or sequential time-stepping is practical (e.g., when spectral methods are employed) [16]. The second approach (equation (2)) does allow for higher density ratios [27, 2], but cannot take advantage of the wide array of efficient solution algorithms for the pressure Poisson equation in incompressible flows. The solution of the variable-coefficient Poisson equation generally requires an iterative scheme, can be an order of magnitude slower, and convergence can be hampered by large density ratios [9]. Finally, in a third approach, for certain flow configurations, it can be practical to eliminate the pressure entirely from the dynamic equations (see Appendix C). This is advantageous because only a cheap, constant-coefficient Poisson solve for the momentum, rather than the pressure, is required and no splitting error is incurred. In all three techniques, the time-dependence of the divergence constraint on the momentum (or velocity) necessitates particular care in enforcing the constraint in the context of the time discretization scheme.

1.2. The Challenging Structure of the Low-Mach Equations

The low-Mach Navier-Stokes equations are a set of partial differential equations in space and time representing conservation of mass and momentum, augmented by a thermodynamic equation of state which directly relates the density to a set of scalar variables for which evolution equations are also written (e.g., temperature and species mass fractions). However, there is a redundancy in the equations since the density must simultaneously obey the equation of state and the mass conservation equation. The

challenge in solving the low-Mach equations numerically is to time advance the equations in a way that preserves the consistency. Inconsistencies between the evolution equations and the equation of state can be numerically destabilizing, as kinetic energy can be incorrectly injected into the system [28]. Shunn and Ham [32] suggest that equations of state that are sufficiently nonlinear can introduce prohibitive resolution requirements on the density even when the other scalar fields are well resolved. In turn, these under-resolved features can produce nonphysical velocity fields. More generally, instability can occur due to inconsistencies that arise when the equations are time advanced in a sequential manner. Knikker [18] notes it is impossible to advance the low-Mach equations in conservative form with such sequential schemes and satisfy the equation of state without some sort of iterative procedure. Instead predictor-corrector approaches are common, since they presumably can lessen, but not eliminate, the degree of the inconsistencies and provide additional stability while being computationally cheaper than a fully-coupled, temporally-implicit scheme. However, these predictor-corrector methods are susceptible to instabilities when density gradients are large [25].

In the work reported here, we address the numerical inconsistency challenges discussed above by reformulating the low-Mach equations to enable explicit time integration while preserving the consistency between the equation of state and the evolution equations (section 2). This is similar in spirit to the algorithm proposed in [20], which also directly enforces this consistency. Here however, by Helmholtz-decomposing the momentum density, a formulation is proposed that consists of a part that can be treated numerically like the constant density incompressible equations, and a modified transport equation that ensures consistency with the equation of state. Further, a novel time-discretization scheme is proposed that allows for incomplete iterative solution of the linear system that arises in this formulation, while preserving the temporal stability and order of accuracy - in this case, second order (section 3). The efficacy of these developments is tested on a Rayleigh-Taylor instability problem with density ratio up to 25.7 (section 4), and finally concluding remarks are provided in section 5. In these developments several choices have been made that are particularly advantageous when used with Fourier spectral discretization in at least two of the three spatial directions. This will be pointed out when it occurs, and alternatives appropriate for more general spatial discretization will be proposed.

2. Governing equations

The low-Mach Navier-Stokes equations can be used with a wide variety of thermodynamic or thermochemical systems, using a spatially-uniform background thermodynamic pressure. To address the numerical inconsistency issues described above, we consider an idealized thermochemical state characterized by a single state variable z. In the simplest case, this might be the temperature or internal energy, but could be, for example, a reaction progress variable or a species mass fraction. The formulation developed here can also be generalized to more complex thermochemical descriptions. The low-Mach-number Navier-Stokes equations representing conservation of mass, momentum, and z for a viscous fluid are, along with the equation of state, given by

$$\frac{\partial \rho}{\partial t} + \frac{\partial \rho u_j}{\partial x_j} = 0$$

$$\frac{\partial \rho u_i}{\partial t} + \frac{\partial}{\partial x_j} (\rho u_i u_j) = -\frac{\partial p}{\partial x_i} + \frac{\partial \tau_{ij}}{\partial x_j}$$

$$\frac{\partial \rho z}{\partial t} + \frac{\partial}{\partial x_j} (\rho u_j z) = \frac{\partial q_j}{\partial x_j} + S_z$$

$$\rho = f(z)$$
(3)

where u_i is the fluid velocity, ρ the density, p the mechanical pressure, τ_{ij} the viscous stress tensor, and q_j is the diffusive flux of z. There may also be a source term S_z in the z equation. For example, if z is the internal energy, S_z is the viscous dissipation of kinetic energy. For a Newtonian fluid with Fickian (or Fourier) diffusive transport of z, the constitutive relations are

$$\tau_{ij} = -\frac{2}{3}\mu \frac{\partial u_k}{\partial x_k} \delta_{ij} + \mu \left(\frac{\partial u_i}{\partial x_j} + \frac{\partial u_j}{\partial x_i} \right)$$

$$q_j = \rho \mathcal{D}_z \frac{\partial z}{\partial x_j}$$
(4)

where μ is the fluid dynamic viscosity, $\rho \mathcal{D}_z$ is the effective diffusivity of z and δ_{ij} is the Kronecker delta. The transport coefficients $\mu = g(z)$ and $\mathcal{D}_z = h(z)$ are assumed to be known functions of z, as is the density through the equation of state $\rho = f(z)$.

As a first step in reformulating the low-Mach equations, consider the Helmholtz decomposition of the momentum $m = \rho u$:

$$\boldsymbol{m} = \boldsymbol{m}^d + \boldsymbol{m}^c \tag{5}$$

where m^d is divergence free and m^c is curl free, so that

$$\boldsymbol{m}^c = \nabla \psi \tag{6}$$

for some scalar potential ψ . With this decomposition, the conservation of mass equation is

$$\frac{\partial \rho}{\partial t} = -\nabla \cdot \boldsymbol{m}^c = -\Delta \psi \,, \tag{7}$$

which represents a constraint on the curl-free momentum. Dynamic equations for m^d can then be expressed as

$$\frac{\partial m_i^d}{\partial t} + \frac{\partial}{\partial x_j} \left(\rho u_i u_j \right) = -\frac{\partial \zeta}{\partial x_i} + \frac{\partial \tau_{ij}}{\partial x_j} \tag{8}$$

where $\zeta = p + \partial \psi / \partial t$. Note that in this formulation ζ is determined to ensure that the divergence of \mathbf{m}^d is zero, but has no direct influence on \mathbf{m}^c .

The eventual time discretization of the z evolution equation is complicated by the fact that the time derivative of z directly determines m^c , and therefore affects the velocities appearing in the z equation. Consider that the equation of state $\rho = f(z)$ and the mass conservation equation imply

$$\frac{\partial \rho}{\partial t} = \frac{df}{dz} \frac{\partial z}{\partial t} = -\nabla \cdot \boldsymbol{m}^c = -\Delta \psi. \tag{9}$$

Since the equation of state determines the density in terms of z, it is useful to rewrite the z evolution equation in its convective form:

$$\rho \frac{\partial z}{\partial t} + (\boldsymbol{m}^d + \boldsymbol{m}^c) \cdot \nabla z = \nabla \cdot \boldsymbol{q} + S_z$$
(10)

where ρu in the convection term has been rewritten as the sum of the divergence-free and curl-free momenta. The fact that m^c can be determined from $\partial z/\partial t$ from equation (9) means that there is an explicit linear dependence of the convection term of equation (10) on $\partial z/\partial t$. This is the root of the challenge of stably time discretizing the low-Mach equations. When naively time advancing the momentum and z equations, z and the momentum will not in general satisfy equation (9), which will be destabilizing, especially when large density variations are present.

To address this challenge, the z equation can be reformulated to explicitly account for the dependence of \mathbf{m}^c on $\partial z/\partial t$. Using equation (9) to express $\partial z/\partial t$ and \mathbf{m}^c in terms of ψ and rearranging, the z transport equation (10) becomes

$$\Delta \psi - \frac{1}{\rho} \nabla \rho \cdot \nabla \psi = -\frac{df}{dz} \mathcal{R}_z \tag{11}$$

where

$$\mathcal{R}_z \equiv \frac{1}{\rho} \left(-\boldsymbol{m}^d \cdot \nabla z + \nabla \cdot \boldsymbol{q} + S_z \right) , \qquad (12)$$

is the modified right-hand side. Thus, given z, m^d , and S_z at any time, the z transport equation can be viewed as an elliptic partial differential equation for ψ . After solving equation (11) for ψ , one can then calculate

$$\frac{\partial z}{\partial t} = -\left(\frac{df}{dz}\right)^{-1} \Delta \psi \ , \ \boldsymbol{m}^c = \nabla \psi \, .$$

Obtaining the z time derivative and m^c in this way ensures consistency between the equation of state, the mass conservation equation, and the z transport equation. Having determined $\partial z/\partial t$, one can use standard explicit methods to time advance z. Having determined m^c one has the total momentum $m^d + m^c$ and therefore the total velocity, allowing the convection terms in the momentum equation

(8) to be computed. Then existing explicit methods for the time discretization of the constant density incompressible equations can be used to time advance equation (8) with ζ (instead of solely p) enforcing the divergence-free constraint.

Before proceeding to discuss the solution of equation (11) it is worth considering how this formulation might be generalized to accommodate a more complex thermochemical description, as the above development appears to rely heavily on the simple thermochemical representation in terms of the single variable z. In the above manipulation, the convective form of the z equation (10) is multiplied by df/dz and divided by ρ , yielding the evolution equation for ρ implied by the z equation:

$$\frac{\partial \rho}{\partial t} + \frac{1}{\rho} \left(\boldsymbol{m}^c + \boldsymbol{m}^d \right) \cdot \nabla \rho = \frac{1}{\rho} \frac{df}{dz} \left(\nabla \cdot \boldsymbol{q} + S_z \right) . \tag{13}$$

Equation (11) is then obtained by substituting for $\partial \rho/\partial t$ and \mathbf{m}^c in terms of ψ from equations (6) and (9). To generalize then, one uses the thermochemical state relation for ρ to transform the transport equations for the thermochemical state variables so that they explicitly include a transport equation for ρ , which will appear redundant with the mass conservation equation. Substituting in terms of ψ will then yield equation (11) with a right-hand side specific to the thermochemical description. In this way a much more complicated thermochemical description can be treated, which may include, for example, chemical reactions with heat release and differential diffusion of species.

For non-trivial problems, solution of equation (11) for ψ will generally require an iterative linear solver. When the Laplacian can be easily inverted, it may be advantageous to recast equation (11) in terms of $\partial \rho / \partial t$ or equivalently $\partial z / \partial t$ using:

$$\psi = -\Delta^{-1} \frac{\partial \rho}{\partial t} = -\Delta^{-1} \left(\frac{df}{dz} \frac{\partial z}{\partial t} \right), \tag{14}$$

where Δ^{-1} is the inverse Laplacian with appropriate boundary conditions. It is thus clear that ψ , $\partial \rho/\partial t$ and $\partial z/\partial t$ carry the same information, and that equation (11) can be rewritten

$$\frac{\partial \rho}{\partial t} - \frac{1}{\rho} \nabla \rho \cdot \nabla \Delta^{-1} \left(\frac{\partial \rho}{\partial t} \right) = \frac{df}{dz} \mathcal{R}_z \tag{15}$$

or equivalently

$$\frac{\partial z}{\partial t} - \frac{1}{\rho} \nabla z \cdot \nabla \Delta^{-1} \left(\frac{df}{dz} \frac{\partial z}{\partial t} \right) = \mathcal{R}_z. \tag{16}$$

In the context of an iterative solution algorithm for equation (11), the inverse-Laplacian can be thought of as a pre-conditioner, to improve convergence. Indeed, in section 3.2, a simple Richardson iteration is proposed to solve equation (16) and used successfully in section 4. Of course, in most cases, the Laplacian cannot be so easily inverted, in which case it would be preferable to solve equation (11) using an appropriately selected iterative solver. One exception is when Fourier spectral discretizations are used in at least two spatial directions, as with the computations reported in section 4.

3. Temporal discretization

The formulation described in section 2 requires a second elliptic solve for ψ (or $\partial z/\partial t$), which is in addition to the elliptic solve required in the equation for m^d (equation (8)). When explicit time discretization methods are used, the elliptic solves dominate the computational cost, so it is important to reduce the cost of this additional solve. The time-discretization approach described here does that by allowing the iterative solution to terminate early while preserving the order of accuracy of the solution. The minimum number of iterations is then dictated by stability rather than temporal accuracy.

The method proposed here is based on the explicit, second-order Runge-Kutta (RK2) scheme with the intent that it can be used for massively parallel calculations. The iterative solution of equation (11) or equation (16) for ψ or $\partial z/\partial t$ is formulated so that the solution for z will be temporally second order regardless of the number of iterations. Rather than controlling temporal accuracy, the number of iterations controls the magnitude of destabilizing inconsistencies between the equation of state, mass conservation equation, and scalar transport equation. The cost is then minimized by reducing the number of solver iterations to the minimum required for stability.

3.1. Incomplete iterative solution

Once spatially discretized, the solution of equation (11) or equation (16) reduces to the solution of a linear algebraic equation of the form:

$$A\mathbf{y} = \mathbf{b} \tag{17}$$

where \mathcal{A} is a square non-singular matrix and \mathbf{y} and \mathbf{b} are column vectors. Assuming that a direct solution of this system is not feasible, we can select an iterative algorithm from a wide variety of such algorithms (see e.g., [3, 31, 12]). Generally for such algorithms, the magnitude of the residual $\mathbf{r}_k = \mathcal{A}\mathbf{y}_k - \mathbf{b}$ at the k^{th} iteration is proportional to the magnitude of $\mathbf{r}_0 = \mathbf{b} - \mathcal{A}\mathbf{y}_0$, where \mathbf{y}_0 is the initial guess. This is clearly true for stationary iterative methods (e.g., Jacobi or Gauss-Seidel) in which the solution error at the k^{th} iteration $\delta \mathbf{y}_k = \mathbf{y}_k - \mathbf{y}$ is given by $\mathcal{C}^k \delta \mathbf{y}_0$ where $\delta \mathbf{y}_0$ is the error in the initial guess, and \mathcal{C} is a matrix determined from \mathcal{A} depending on the particular algorithm being used. Trivially, the residual sequence also satisfies $\mathbf{r}_k = \mathcal{C}^k \mathbf{r}_0$. For Krylov subspace methods (e.g., conjugate gradient, GMRES), \mathbf{r}_k is the remainder after the initial residual \mathbf{r}_0 is projected onto the Krylov subspace. Thus the magnitudes of \mathbf{r}_k and $\delta \mathbf{y}_k$ also scale with the magnitude of \mathbf{r}_0 .

The consequence of this property of iterative liner solvers is that if the linear solution is part of a time discretization and we arrange for the initial guess \mathbf{y}_0 to have an order Δt^n error, where Δt is the discretization time step, the solution at each iteration will also have an order Δt^n error. In this case, the linear solver iterations can be terminated early to reduce costs while not impacting the temporal order of accuracy.

3.2. A time-accurate initial guess

The linear system of relevance here arises from the spatial discretization of the z equation, whether expressed in terms of ψ , $\partial \rho/\partial t$, or $\partial z/\partial t$. The matrix \mathcal{A} is then a spatially discrete representation of the operator on the left-hand side of equations (11), (15) or (16), and b represents the right-hand side. To apply the incomplete iteration scheme described above, we thus need to develop an order Δt^2 approximation of ψ , $\partial \rho/\partial t$, or $\partial z/\partial t$, depending on the formulation used. For specificity, the formulation in equation (16) for $\partial z/\partial t$ is considered here. Similar schemes can be developed for the other formulations.

To simplify the presentation, let $\mathcal{I} - \mathcal{L}$ be the matrix representing the spatial discretization of the linear operator acting on $\partial z/\partial t$ on the left-hand side of equation (16). That is

$$\mathcal{L}(\tilde{z})\frac{d\tilde{z}}{dt} \approx \frac{1}{\rho}\nabla z \cdot \nabla \Delta^{-1} \left(\frac{df}{dz}\frac{\partial z}{\partial t}\right)$$
(18)

where \tilde{z} is the spatially discrete representation of z. The spatial discretization of equation (16) then reads

$$(\mathcal{I} - \mathcal{L}(\tilde{z})) \frac{d\tilde{z}}{dt} = \widetilde{\mathcal{R}}_z \tag{19}$$

where \mathcal{L} is clearly depends on the current \tilde{z} and $\widetilde{\mathcal{R}}_z$ is the spatial discretization of \mathcal{R}_z from equation (16). To time advance \tilde{z} , equation (19) must be solved for $d\tilde{z}/dt$. While any number of iterative linear solvers could be used for this purpose, here a simple Richardson iterative algorithm given by

$$\frac{d\tilde{z}^{k}}{dt} = \mathcal{L}(\tilde{z})\frac{d\tilde{z}^{k-1}}{dt} + \tilde{\mathcal{R}}_{z}$$
(20)

is used. Provided the spectral radius of \mathcal{L} is less than one, this iteration will converge to the solution for $d\tilde{z}/dt$. However, to reduce computational cost, we propose here to terminate this iteration early. To preserve the second-order temporal accuracy of the RK2 scheme used to time-advance the \tilde{z} equation, the error in $d\tilde{z}/dt$ must scale as Δt^2 . As discussed in section 3.1, to ensure this accuracy it is sufficient to select an initial guess such that the error in $(d\tilde{z}/dt)^0$ scales with Δt^2 . Then regardless of the number of iterations, the expected time accuracy will be attained, so that only as many iterations as is required to assure stability are needed, as discussed below.

To advance in time from t_n to $t_{n+1} = t_n + \Delta t$, the RK2 time discretization requires that the time derivative be evaluated at time t_n and at an intermediate time $t_{n+1/2} = t_n + \Delta t/2$. Call the time derivative evaluated at these times $(d\tilde{z}/dt)^n$ and $(d\tilde{z}/dt)^{n+1/2}$, respectively. An initial guess for the iterative solution of equation (16) for $d\tilde{z}/dt$ at these times can be determined from past values of \tilde{z} using

a backwards difference-type formulation, as follows:

$$\Delta t \frac{d\tilde{z}^{n,0}}{dt} = 2\tilde{z}^n - 2\tilde{z}^{n-1/2}$$

$$\Delta t \frac{d\tilde{z}^{n+1/2,0}}{dt} = \left(4 + \beta^{n+1/2}\right) \tilde{z}^{n+1/2} - \left(5 + 2\beta^{n+1/2}\right) \tilde{z}^n + \beta^{n+1/2} \tilde{z}^{n-1/2} + \tilde{z}^{n-1}$$
(21)

where $\beta^{n+1/2}$ is a free parameter. As shown in Appendix A, the $d\tilde{z}/dt$ estimates in equation (21) are accurate to $\mathcal{O}(\Delta t^2)$. Note that while the discretization used here is RK2, in principle a similar approach could be used for third (or higher) order discretizations. However, this would require past values of z at more time levels to retain higher order accuracy in the backward difference formulation of initial guesses. This would introduce additional parasitic modes in the backward difference formula, with potential negative impacts on stability, which would need to be addressed.

In addition to time advancing the z equation, $d\tilde{z}/dt$ is used to determine the spatially discrete curl-free momentum $\widetilde{\boldsymbol{m}}^c$ from equation (14):

$$\widetilde{\boldsymbol{m}}^c = -\nabla \Delta^{-1} \left(\frac{df}{dz} \frac{d\tilde{z}}{dt} \right). \tag{22}$$

A temporally second-order approximation to $d\tilde{z}/dt$ at any time level therefore also yields a temporally second-order approximation to $\widetilde{\boldsymbol{m}}^c$ at that time level.

3.3. A simple test case

To see how the time discretization described in section 3.2 is applied and to explore its accuracy and stability, consider a simple system of ODEs that with characteristics similar to the low-Mach-number, variable density equations.

$$(1 - \mathcal{M}_1(z)) \frac{dz}{dt} = \mathcal{M}_2(z)$$

$$\frac{dm^d}{dt} = \mathcal{M}_3(m^d, m^c)$$

$$\frac{d\rho}{dt} = \mathcal{G}(m^c)$$

$$\rho = f(z)$$
(23)

where $\mathcal{M}_3(m^d,m^c)$ is nonlinear in both m^d and m^c and is a surrogate for the momentum equations (equation (8)). \mathcal{G} is a linear operator acting on m^c akin to the divergence operator in the mass conservation equation. In the z equation, \mathcal{M}_1 is a z-dependent linear operator acting on dz/dt and \mathcal{M}_2 is nonlinear in z – this equation has the same structure as equation (19) with \mathcal{M}_1 playing the role of \mathcal{L} and \mathcal{M}_2 the role of \mathcal{R}_z .

For an arbitrary stage $s \in \{n, n+1/2\}$ and a chosen number of linear solver iterations k^f , $(z^s, m^{d,s}, m^{c,s})$ are updated by algorithm 1.

3.3.1. Temporal convergence tests

To verify the order of accuracy of the temporal scheme, numerical solutions of system (23) are sought with

$$\mathcal{M}_1(z) = c_1 (1 + \sin(z)) , \quad \mathcal{M}_2(z) = c_2 \exp(z) , \quad \mathcal{M}_3(m^d, m^c) = c_3 m^d (m^c)^3 ,$$

$$\mathcal{G}(m^c) = c_4 m^c , \quad f(z) = z ,$$
(24)

where $c_1 = .6i$, $c_2 = -1$, $c_3 = 2 - .8i$, $c_4 = -3 + .5i$. The initial conditions for z and m^d are $z_0 = m_0^d = .5$. A reference solution is obtained by inverting $1 - \mathcal{M}_1$ directly and integrating

$$\frac{dz}{dt} = \frac{\mathcal{M}_2(z)}{1 - \mathcal{M}_1(z)} \,. \tag{25}$$

To control temporal errors in the reference solution a fine $\Delta t = 1 \times 10^{-9}$ is used, an order of magnitude lower than the final test case shown here. To ensure consistency of the initial condition for the test cases

Algorithm 1 Time advancement of system (23)

1: Start with
$$m^{d,s}, m^{c,s}, \frac{dz}{dt}^{s,k^f}, \frac{dz}{dt}^{s-1/2,k^f}, \mathcal{M}_3(m^{d,s-1/2}, m^{c,s-1/2})$$
 from previous stages, evaluate

$$\mathcal{M}_3(m^{d,s}, m^{c,s}).$$

2: Using
$$\frac{dz}{dt}^{s,k^f}$$
, $\frac{dz}{dt}^{s-1/2,k^f}$, advance $z^s \to z^{s+1/2}$ with RK2.

3: Using
$$\mathcal{M}_3(m^{d,s}, m^{c,s})$$
, $\mathcal{M}_3(m^{d,s-1/2}, m^{c,s-1/2})$, advance $m^{d,s} \to m^{d,s+1/2}$ with RK2.

4: Generate initial guess
$$\frac{dz^{s+1/2,0}}{dt}$$
 as shown in equation (21).

5:
$$k = 0$$

6: **for**
$$k <= k_f$$
 do

7:
$$\frac{dz^{s+1/2,k}}{dt} = \mathcal{M}_1(z^{s+1/2}) \frac{dz^{s+1,k-1}}{dt} + \mathcal{M}_2(z^{s+1})$$

8: end for

9: Evaluate
$$\frac{d\rho}{dt}^{s+1} = \frac{df}{dz}(z^{s+1})\frac{dz}{dt}^{s+1,k_f}$$
, solve for $m^{c,s+1} = \mathcal{G}^{-1}\frac{d\rho}{dt}^{s+1}$.

and reference solution, m_0^c is specified as

$$m_0^c = \mathcal{G}^{-1} \left[\frac{df}{dz} \frac{\mathcal{M}_2}{1 - \mathcal{M}_1} \right]_{z=z_0} . \tag{26}$$

The backward difference parameter is set to $\beta^{n+1/2} = -4$ (equation (21)) for generating the initial guesses for the iterative linear solution.

Figure 1 shows the convergence rate of z and m^d for the test problem with both double and extended (long double) precision by comparing the solution at t=.1 to the reference solution. Four iterations $(k^f=4)$ are used to solve the z equation at each substep. Some noise in the error is expected close to machine precision; however, the behavior seen for small Δt needs further explanation. Round-off errors in z are amplified during the estimation of dz/dt from the time history of z because a linear combination of the four previous evaluations is scaled by $1/\Delta t$ (see equation (21)). These errors affect m^c and, in turn, can degrade the apparent convergence rate of m^d and z. In extended precision (long double) calculations second-order convergence continues to smaller Δt (figure 1), which demonstrates that the convergence floor in the double precision result is solely a consequence of round-off error.

3.3.2. Linear stability analysis

To assess the stability of this algorithm, consider a linearized system modeling the characteristics of the z equation in system (23)

$$(1 - \lambda_1) \frac{dz}{dt} = \lambda_2 z \tag{27}$$

where $\lambda_1, \lambda_2 \in \mathbb{C}$. Additionally, define $\lambda^* \equiv \frac{\lambda_2}{1 - \lambda_1}$ so that

$$\frac{dz}{dt} = \lambda^* z \tag{28}$$

is the underlying modified ODE (assuming $\lambda_1 \neq 1$). In this context, setting $\lambda_2 = 0$ in equation (27) yields the test problem to assess zero stability (see below).

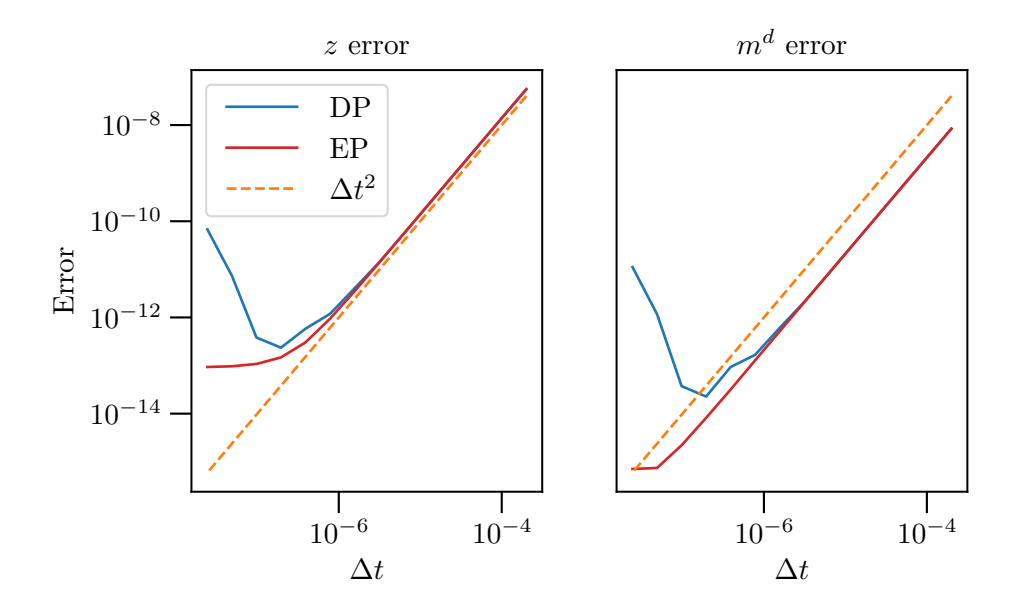


Figure 1: Convergence of the proposed time discretization scheme (algorithm 1) applied to the model problem defined in system (23) and equation (24). Shown are errors in computed z (left) and m^d (right) at t = 0.1, relative to the reference solution defined in equation (25). Calculations were done in double precision (DP) and long double, extended precision (EP).

Applying the temporal scheme with k linear iterations to equation (27) gives

$$z^{n+1/2,k} - z^{n} = \lambda_{1}^{k} \left\{ z^{n} - z^{n-1/2} \right\} + \frac{1}{2} \Delta t \sum_{j=0}^{k-1} \lambda_{1}^{j} \lambda_{2} z^{n}$$

$$z^{n+1,k} - z^{n+1/2} = \lambda_{1}^{k} \left\{ \left(3 + \beta^{n+1/2} \right) z^{n+1/2} - \left(6 + 2\beta^{n+1/2} \right) z^{n} + \left(\beta^{n+1/2} + 1 \right) z^{n-1/2} + z^{n-1} \right\}$$

$$+ \Delta t \sum_{j=0}^{k-1} \lambda_{1}^{j} \lambda_{2} \left(z^{n+1/2} - \frac{1}{2} z^{n} \right) .$$

$$(29)$$

Taking inspiration from linear differential equation analysis [22], this can be written as $z^{n+1} = A_1 A_2 z^n = A z^n$ where $z^n = \begin{bmatrix} z^n & z^{n-1/2} & z^{n-1} & z^{n-3/2} \end{bmatrix}^T$ (the matrices are detailed in Appendix B). For $\rho(A) < 1$, the scheme is linearly stable.

Unlike traditional explicit Runge-Kutta methods designed for ODEs of the form dz/dt = f(z) (like equation (28)), the scheme is not unconditionally zero stable (that is, stable with $\lambda_2 = 0$). In this case, λ_1 , the choice of $\beta^{n+1/2}$, and the number of iterations impact the zero stability. The initial guesses for dz/dt introduce parasitic modes (akin to linear multistep methods) which are damped by each linear iteration if and only if $\|\lambda_1\| < 1$. Generally, the size of the zero stability regions grows with the number of iterations for a given $\beta^{n+1/2}$ when $\|\lambda_1\| < 1$ (figure 2.(a)). When fully converged, the zero-stability region is a circle of radius 1, which is consistent with the scheme diverging for $\rho(\mathcal{M}_1) \geq 1$ and recovering the stability properties of RK2 otherwise. Setting $\beta^{n+1/2} = -4$ yields the optimal zero-stability region (circle of radius 1) regardless of the number of iterations (figure 2.(b)), therefore $\beta^{n+1/2} = -4$ is used to obtain all results from hereon out.

The absolute-stability region is defined in terms of the "true" eigenvalue, λ^* , and is plotted for different values of λ_1 , see figure 3. As expected, when fully converged the absolute stability region coincides with the standard RK2 result. For small $\|\lambda_1\|$ this convergence happens quickly so that only two or three iterations are required for a stability region that approaches that of RK2. As the eigenvalue magnitude approaches one, as in figure 3.d, around ten iterations are needed for the stability region to near that of RK2. The type of analysis shown here can be used as a heuristic to determine an appropriate number of linear iterations if an estimate of the largest eigenvalues of \mathcal{L} is obtained a priori.

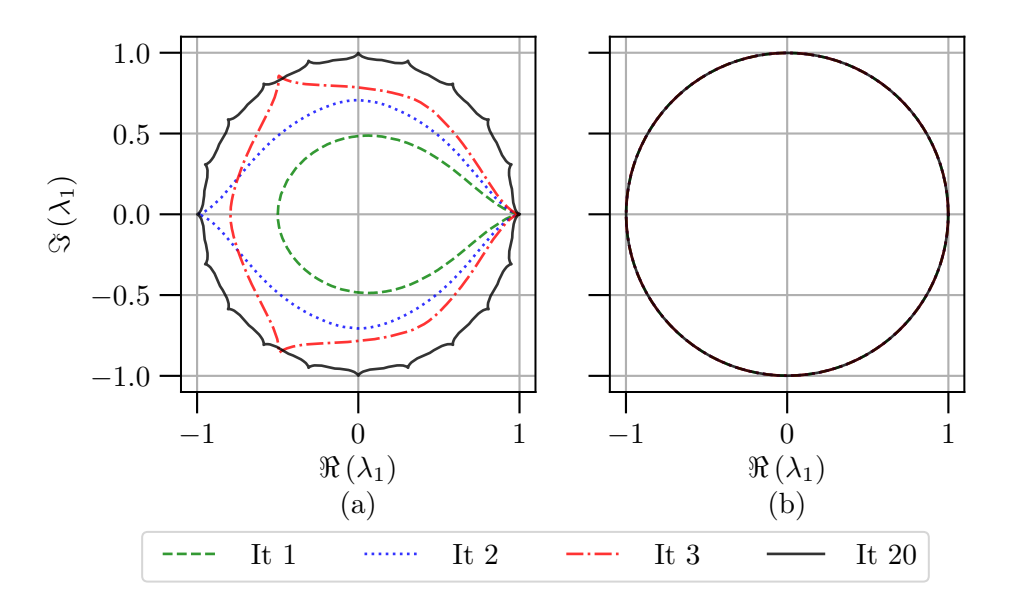


Figure 2: Zero stability region of the proposed temporal discretization applied to equation (27) (i.e., with $\lambda_2=0$) as a function of the number of linear solver iterations for $\beta^{n+1/2}=-1$ (left) and $\beta^{n+1/2}=-4$ (right). For $\beta^{n+1/2}=-4$, the stability region is independent of the number of iteration and always optimal.

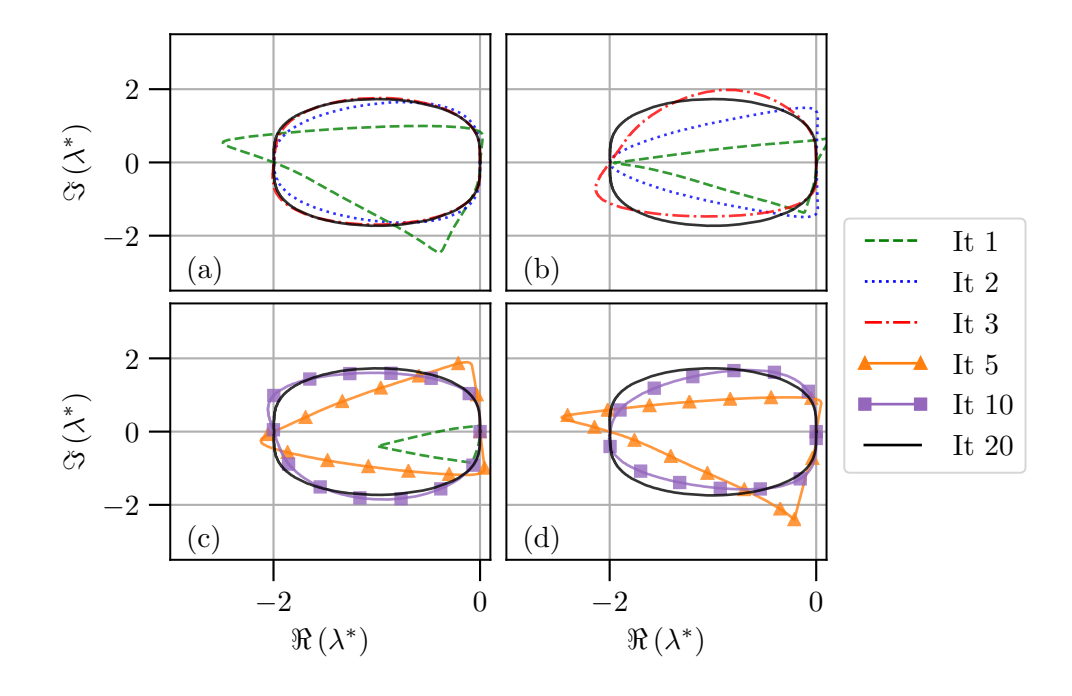


Figure 3: Absolute stability of the proposed temporal discretization applied to equation (27) as a function of the number of iterations for varying λ_1 . (a): $\lambda_1 = .2i$ (iters. 5, 10 not shown), (b): $\lambda_1 = .4i$ (iters. 5, 10 not shown), (c): $\lambda_1 = .5 + .5i$ (iters. 2,3 not shown), (d): $\lambda_1 = .7 + .25i$ (iters. 2,3 not shown – not stable for 1 iter.).

4. Results

To demonstrate the utility of the scheme introduced in section 3, it is incorporated into an algorithm for direct numerical simulation (DNS) of the variable-density, low-Mach Navier-Stokes equations, which is briefly described first. Then a single-mode Rayleigh-Taylor (RT) instability is simulated over a range of Atwood numbers to verify that the algorithm is obtaining solutions to the variable-density equations and explore its stability with respect to density ratio.

The algorithm (detailed in Appendix C) is an extension of the pseudospectral scheme of Kim, Moin, and Moser (KMM) [17] developed for incompressible flows. In their scheme, equations for one component of the vorticity and the Laplacian of the velocity are advanced, eliminating the need to solve for the pressure. Here, we define $\phi \equiv \Delta m^d$ and $\Omega \equiv \nabla \times m^d$ and manipulate the momentum equations (by taking the curl and double curl, which eliminates the pressure) to obtain equations for ϕ_2 and Ω_2 , the components of these quantities in the direction in which periodic boundary conditions are not applied. The equations for ϕ_2 , Ω_2 , and z are time advanced, along with the planar averages of m_1 and m_3 (averaged in the x_1 and x_3 directions). Equation (9) constrains the curl-free momentum, m^c . A similar momentum decomposition was used in the work of Almagro et al. [1]. Their scheme, however, is only first-order accurate in time despite using three RK stages and assumes constant fluid viscosity, thermal conductivity, and specific heat. The algorithm employed here relaxes these restrictive assumptions, achieves a higher-order temporal accuracy in two stages, and a priori guarantees discrete conservation of mass (see Appendix C.2). The temporal scheme (section 3) is fully explicit, which enables efficient use of parallelization, which is necessary for the large problem sizes encountered in, e.g., the direct numerical simulation of turbulence.

At the same time, the formulation of the z equation and the determination of m^c as outlined in section 2 enable stable solutions for density ratios up to at least 25.7, as shown in the RT test problems described here. When using the simple linear solver described in section 3.2, significantly larger density ratios lead to instabilities. It appears that this occurs because the spectral radius of \mathcal{L} defined in equation (18) increases as the density ratio increases. The result is that at high density ratio, the simple Richardson iteration cannot produce sufficiently accurate solutions to equation (19) to ensure stability. We thus expect that a more sophisticated linear solver will allow stable computation at much larger density ratios. None-the-less, the density ratio of 25.7 used here is already much larger than typical for explicit methods.

For spatial discretization, the solution is represented using a Fourier bases in the x_1 and x_3 (streamwise and spanwise) directions, in which periodic boundary conditions are applied, and high-order B-splines [5, 4] in the x_2 direction. Our implementation has been verified (results not shown) with a manufactured solution created with MASA [21], a C++ library that generates source terms for arbitrary differential equations by automatic differentiation. Additionally, we verify the temporal order of accuracy through Richardson extrapolation for one of the RT cases studied below (see additionally Appendix D). An earlier version of this algorithm was implemented for a combustion DNS in [30].

4.1. Single mode Rayleigh-Taylor test problem

Following the setup in, e.g., [15, 14, 19] of a single-mode Rayleigh-Taylor instability in a rectangular box with square cross-section, we consider two fluids of differing density arranged with the heavier fluid on top. They evolve under the influence of gravity, which is aligned with the vertical direction (x_2) . The dynamic viscosity of the two fluids is taken to be the same as in [14] and to account for gravity, a body force is added to the momentum equation in (3) as follows:

$$\frac{\partial \rho u_i}{\partial t} + \frac{\partial \rho u_i u_j}{\partial x_j} = -\frac{\partial p}{\partial x_i} + \frac{\partial \tau_{ij}}{\partial x_j} - \rho g \delta_{i2}. \tag{30}$$

We assume the fluids are miscible and simple binary, Fickian diffusion holds such that

$$z = \frac{\rho_h}{\rho_h - \rho_l} \left(1 - \frac{\rho_l}{\rho} \right) \,, \tag{31}$$

which represents the volumetric mixing of the heavy and light fluids, satisfies the convection-diffusion equation in system (3). Rearranging equation (31), the equation of state is

$$\rho = \frac{\rho_l \rho_h}{\rho_h - (\rho_h - \rho_l)z} \,. \tag{32}$$

The Atwood number characterizes the density contrast between the heavy fluid, ρ_h , and light fluid, ρ_l , and is given by

$$At = \frac{\rho_h - \rho_l}{\rho_h + \rho_l} \implies \frac{\rho_h}{\rho_l} = \frac{1 + At}{1 - At}.$$
 (33)

Computations are performed in both two and three dimensions, in a horizontally periodic domain of size W or $W \times W$. In the vertical (x_2) direction the domain is $x_2 \in [-2W, 2W]$ or [-3.5W, 3.5W], with the larger domains used for high Atwood number (At) cases.

A Fourier representation with 128 modes is used in the periodic directions $(x_1 \text{ and } x_3)$, and in the x_2 direction, either 512 (smaller domain) or 1024 (larger box) B-spline degrees of freedom are employed (see Appendix D for a mesh convergence study). Note that the resolution in the large and small domains is approximately equal. The B-splines are order 8 for all variables except the x_2 component of the momentum, which is order 9 to ensure discrete conservation of mass (see Appendix C.2). In general, the timestep is chosen such that $\Delta t \sqrt{At}/\sqrt{W/g} = 2.5 \times 10^{-4}$, although there are a few exceptions for higher Atwood number cases due to viscous stability constraints. Appendix D includes the grid and timestep for each case presented here.

The initial z is given by

$$z = \frac{1}{2} \left[1 + \tanh\left(\frac{x_2 - h}{2\epsilon W}\right) \right] \tag{34}$$

where $\epsilon = 0.05$ and h is one of:

$$\frac{h^{3D}(x_1, x_3)}{W} = 0.05 \left[\cos \left(\frac{2\pi x_1}{W} \right) + \cos \left(\frac{2\pi x_3}{W} \right) \right] + \delta \tag{35}$$

$$\frac{h^{2D}(x_1)}{W} = 0.1 \left[\cos \left(\frac{2\pi x_1}{W} \right) \right] + \delta \tag{36}$$

for the three- and two-dimensional cases, respectively. At low At, when the smaller vertical domain is used, the offset $\delta=0$. But, at higher At, for which the larger domain is used, $\delta=0.5$ because the heavy fluid penetrates more rapidly into the light fluid. An example of the initial z field can be seen in the leftmost panel of figure 4.

In the cases computed here the Schmidt number is taken to be unity (Sc = 1), so in system (3), $\rho \mathcal{D}_z = \mu$ is constant. A Reynolds number for this problem can be defined in terms of the heavy fluid density, the wavelength W of the initial perturbation, and the acceleration of gravity; that is, $Re = \rho_h \sqrt{W^3 g}/\mu$, which is set to 3000 for the 2D cases and 1024 for the 3D cases reported here.

To ensure that the initial condition is consistent with conservation of mass, the velocity field is prescribed as

$$\frac{\boldsymbol{u}}{\sqrt{Wg}} = -\frac{1}{ReSc} \frac{1}{\rho} \frac{d\rho}{dz} \nabla z. \tag{37}$$

As described in Appendix C.4, potential matching boundary conditions are specified at the top and bottom boundary for the fluctuating momentum, the mean momentum obeys a homogeneous Neumann condition for the spanwise and streamwise components, and a homogeneous Dirichlet boundary condition is specified for the vertical component. A homogeneous Neumann boundary condition is also used for z.

The single-mode RT flow evolves through several stages: first, there is an initial acceleration when viscous effects dominate followed by the formation and growth of a "spike" of heavy fluid traveling downwards along with "bubbles" of light fluid penetrating upwards into the heavy fluid (figure 4). Next, a period of near constant bubble and spike velocity predicted by potential theory occurs before a reacceleration (see, e.g., figure 6). To verify the fidelity of the new algorithm, we compare simulation results to the theoretical result of Goncharov [11], which gives the bubble velocity, or the rate at which the light fluid penetrates the heavy, during the potential growth phase as

$$v_b = \sqrt{\frac{2At}{1+At}} \frac{g}{Ck} \tag{38}$$

where C=1 in three-dimensional flows and 3 in two-dimensional flows and $k=2\pi/W$ is the perturbation wave number. Additionally, comparisons to other results from the literature were made for the bubble/spike trajectories.

To begin, we consider two validation cases found frequently in the literature. The first is a 2D case with At = .5 and Re = 3000 and the second is a 3D case with At = 0.5 and Re = 1024. The evolution

of bubble and spike locations from the current calculations are in good agreement with recent results from Hamzehloo et al. [14], as shown in figure 5. Furthermore, contours of density for the 2D case

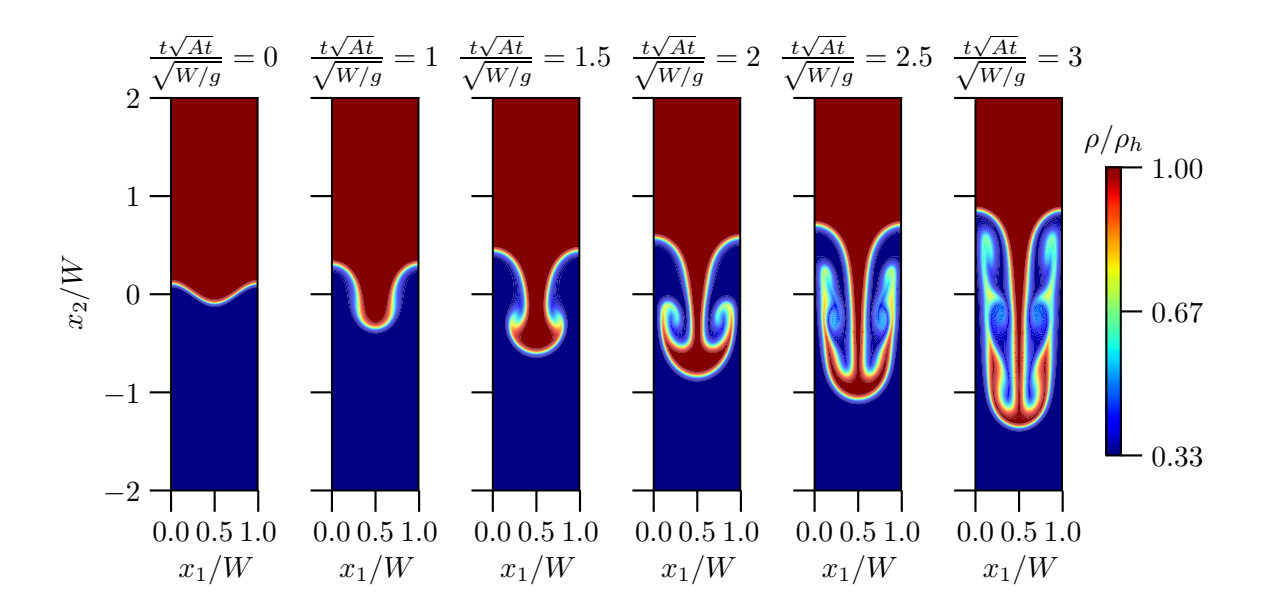


Figure 4: Contours of density at several times in the two-dimensional Rayleigh-Taylor test problem (Re = 3000) with At = 0.5.

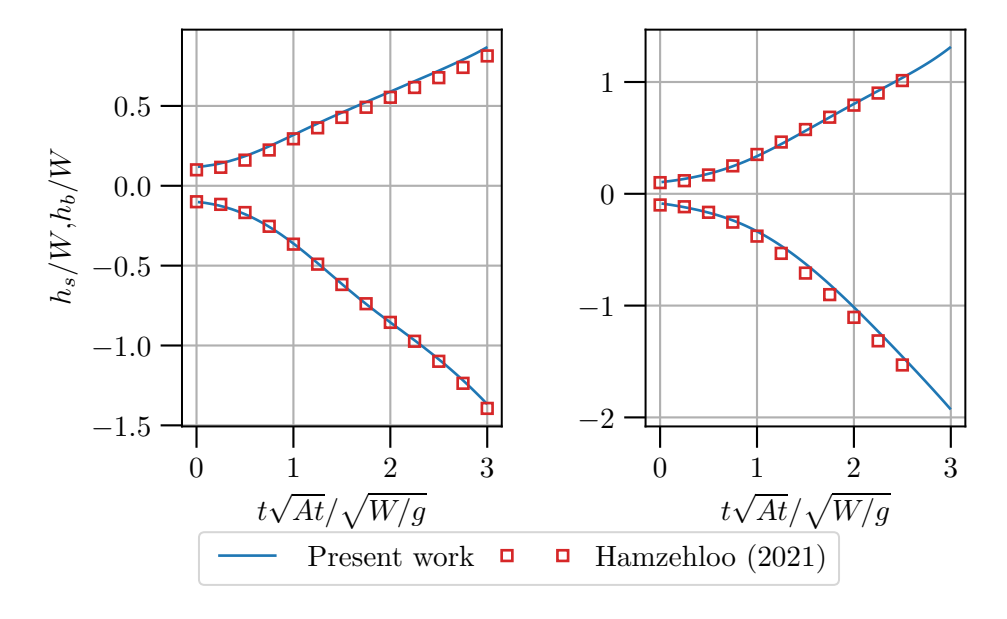


Figure 5: Evolution of the bubble and spike height (h_b, h_s) in the Rayleigh-Taylor test problem with At = 0.5 in two dimensions (left, Re = 3000) and three dimensions (right Re = 1024). Also shown are the bubble and spike evolution from Hamzehloo [14] in both two and three dimensions.

(figure 4) are in good qualitative agreement with previous results [14, 8]. As these previous results were for immiscible fluids, minor discrepancies are expected.

Next, we explore the current algorithm's stability for increasing density ratios by considering a range of Atwood number from 0.33 to 0.925, for both two- and three-dimensional flows. The maximum Atwood number corresponds to a density ratio of 25.67. The bubble and spike evolution vary with Atwood number as expected (figures 6 and 7). Note that the bubble velocity during the potential growth phase, when the velocity is approximately constant, is roughly consistent with the potential theory equation (38).

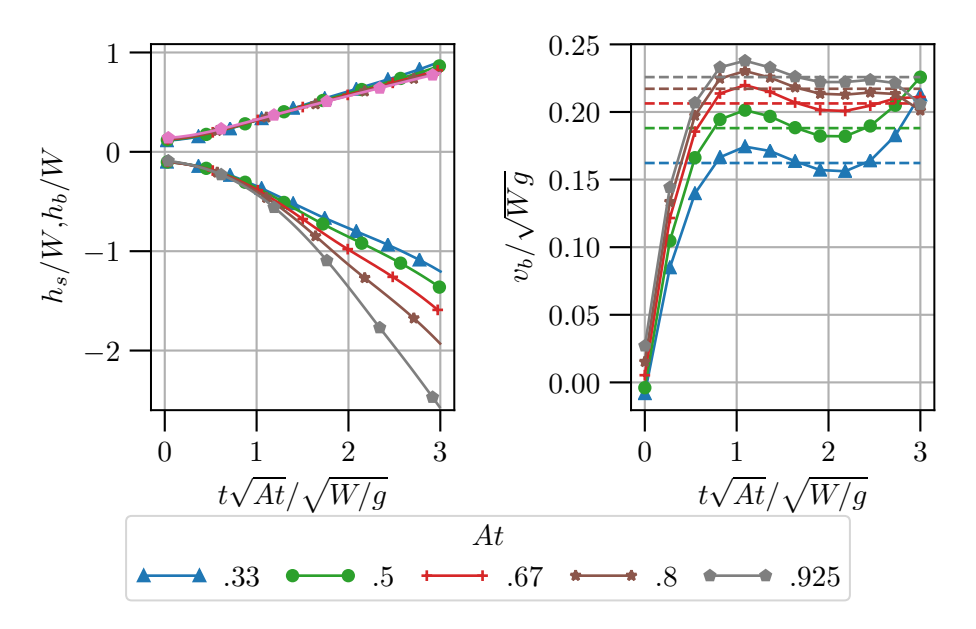


Figure 6: Evolution of the bubble and spike height (h_b, h_s, left) and bubble velocity (v_b, right) for various Atwood numbers in the two-dimensional Rayleigh-Taylor test problem (Re = 3000). Dashed horizontal lines are the velocity given by potential theory, equation (38).

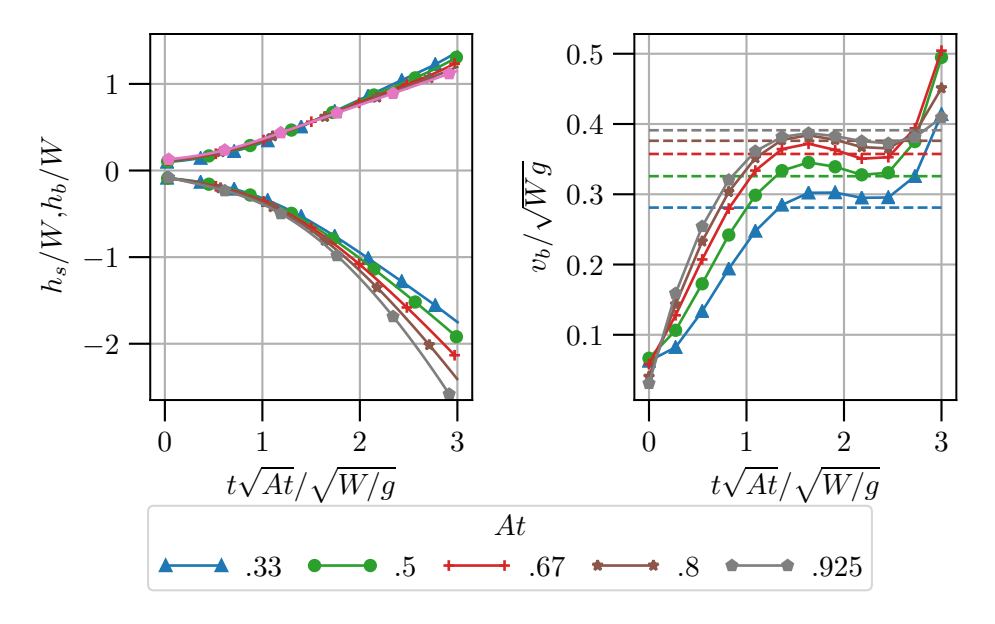


Figure 7: Left: Evolution of the bubble and spike height (h_b, h_s, left) and bubble velocity (v_b, right) for various Atwood numbers in the three-dimensional Rayleigh-Taylor test problem (Re = 1024). Dashed horizontal lines are the velocity given by potential theory, equation (38).

This consistency, along with the consistency with [14] shown in figure 5, suggests that the algorithm is solving the variable-density equations as intended. The minor discrepancies with potential theory can be attributed to the difference between the potential flow model and variable-density Navier-Stokes. These results also demonstrate the algorithm's stability over a wide range of density ratios.

5. Conclusions

A new temporal discretization technique for the low-Mach, variable-density Navier-Stokes equations has been developed. The method is designed to preserve stability for explicit time discretizations. The

challenge was to treat the redundancy between the mass conservation equation, the transport equation(s) for the scalar(s) that characterize the thermochemical state of the fluid (e.g., temperature, chemical species, or mixture fraction) and the equation of state. This redundancy is made most apparent when one considers the evolution equation for the density that is implied by the evolution of the thermochemical state, yielding a second evolution equation for the density as in equation (13), in addition to the mass conservation equation. Ensuring that these two equations for the density are compatible requires that the potential defining the curl-free momentum satisfy an elliptic equation derived from the two density equations, as in equation (11). This formulation suggests that the low-Mach variable density Navier-Stokes equations embody two distinct elliptic effects that must be accounted for, one that ensures the compatibility of the redundant evolution equations for the density and one that ensures that the divergence-free momentum is divergence free, as in the constant density incompressible equations. The stability of the temporal discretization proposed here arises from recognizing this fact, and explicitly solving both elliptic equations.

Generally the elliptic problems will need to be solved iteratively, especially in three dimensions. To mitigate the cost of solving two elliptic equations, it is desirable to minimize the number of iterations needed. To this end, the iterative algorithm for the curl-free momentum potential was integrated with the time discretization so that a temporal extrapolation of the solution from previous time steps could be used to define an initial guess for the iterative algorithm, with error consistent with the temporal order of accuracy of the discretization. This has the dual benefit of producing a small initial error so that the number of iterations required for any desired solution accuracy is reduced, and of ensuring that no matter how many or few iterations are used, the scheme will retain its temporal order of accuracy. The number of iterations can then be determined from stability considerations, rather than temporal order of accuracy.

To demonstrate its utility and explore its stability, the temporal discretization was incorporated into a pseudospectral low-Mach variable density solver and tested on a series of single-mode Rayleigh-Taylor instability problems. It was found to yield stable solutions for density ratios up to at least 25.7 that are both converged and consistent with available theoretical and previous computational results. This new formulation greatly increases the density ratios that can be treated without resorting to fully coupled implicit solvers [25, 18], which can be cost prohibitive. The algorithm may thus be useful for simulation of low-speed turbulent combustion and low-speed turbulent mixing of fluids with different densities. Direct simulation of turbulent combustion is the application that motivated the current developments.

In the test cases reported here, the proposed temporal discretization was applied using pseudospectal methods in doubly periodic domains on a problem with a simple representation of the thermochemical state in terms of a single scalar variable. These features allowed for several simplifications, and so continued development of the proposed discretization should be directed at removing these simplifications. First, the evolution of the divergence-free momentum was formulated to solve an elliptic equation for one of the momentum components as in [17], rather than for the pressure variable as is common in pressure projection methods. Such pressure projection methods often incur splitting errors, and the consequences of this error on the stability characteristics of the proposed scheme needs to be investigated. Second, the ability to efficiently solve the Poisson equation in the pseudospectral method allowed the elliptic solve for the curl-free momentum potential to be effectively preconditioned so that a simple iterative algorithm could be used. More sophisticated matrix-free algorithms need to be explored for use when spectral methods are not used. Third, it may be possible to refine the time discretization and/or the backward difference scheme used to obtain an initial guess for the iterative solver to attain either better stability or higher accuracy, and this would be worth pursuing. Finally, the generalization of the algorithm outlined at the end of section 2 needs to be applied to enable the use of more complex representations of the thermochemical state that include many scalar evolution equations and, therefore, can represent more complex phenomena such as chemical reactions with heat release.

6. Acknowledgments

This article has been authored by an employee of National Technology & Engineering Solutions of Sandia, LLC under Contract No. DE-NA0003525 with the U.S. Department of Energy (DOE). The employee owns all right, title and interest in and to the article and is solely responsible for its contents. The United States Government retains and the publisher, by accepting the article for publication, acknowledges that the United States Government retains a non-exclusive, paid-up, irrevocable, world-wide license to publish or reproduce the published form of this article or allow others to do so, for United States Government

purposes. The DOE will provide public access to these results of federally sponsored research in accordance with the DOE Public Access Plan

https://www.energy.gov/downloads/doe-public-access-plan. This paper describes objective technical results and analysis. Any subjective views or opinions that might be expressed in the paper do not necessarily represent the views of the U.S. Department of Energy or the United States Government.

A. Obtaining the BDF-like approximations

The BDF-like approximations from section 3 are generated by assuming the available time history of z matches the progression of a variable time advanced by RK2. That is,

$$z^{n+1} = z(t_n) + \Delta t \frac{dz}{dt} \Big|_{t_n} + \frac{1}{2} \Delta t^2 \frac{d^2z}{dt^2} \Big|_{t_n} + \mathcal{O}\left(\Delta t^3\right)$$

$$z^{n+1/2} = z(t_n) + \frac{1}{2} \Delta t \frac{dz}{dt} \Big|_{t_n} + \mathcal{O}\left(\Delta t^3\right)$$

$$z^n = z(t_n)$$

$$z^{n-1/2} = z(t_n) - \frac{1}{2} \Delta t \frac{dz}{dt} \Big|_{t_n} + \mathcal{O}\left(\Delta t^3\right)$$

$$z^{n-1} = z(t_n) - \Delta t \frac{dz}{dt} \Big|_{t_n} + \frac{1}{2} \Delta t^2 \frac{d^2z}{dt^2} \Big|_{t_n} + \mathcal{O}\left(\Delta t^3\right)$$

$$z^{n-3/2} = z(t_n) - \frac{3}{2} \Delta t \frac{dz}{dt} \Big|_{t_n} + \Delta t^2 \frac{d^2z}{dt^2} \Big|_{t_n} + \mathcal{O}\left(\Delta t^3\right),$$

$$z^{n-3/2} = z(t_n) - \frac{3}{2} \Delta t \frac{dz}{dt} \Big|_{t_n} + \Delta t^2 \frac{d^2z}{dt^2} \Big|_{t_n} + \mathcal{O}\left(\Delta t^3\right),$$

where Taylor expansions about t_n have been used.

A.1. Coefficients for fixed-point problem

We seek an approximation which is accurate up to $\mathcal{O}\left(\Delta t^2\right)$ to initialize the first stage fixed-point iteration (equation (20)). At this stage, $z^n, z^{n-1/2}, z^{n-1}, z^{n-3/2}$ are available. Let

$$\Delta t \frac{dz}{dt}^{n,0} = \alpha_1^n z^n + \alpha_2^n z^{n-1/2} + \alpha_3^n z^{n-1} + \alpha_4^n z^{n-3/2} = \Delta t \frac{dz}{dt} \bigg|_{t_n} + \mathcal{O}\left(\Delta t^3\right)$$
(A.2)

where the α 's are a set of weights. By matching the lower-order terms in the Taylor expansions, it follows that

$$\alpha_1^n + \alpha_2^n + \alpha_3^n + \alpha_4^n = 0$$

$$-\frac{1}{2}\alpha_2^n - \alpha_3^n - \frac{3}{2}\alpha_4^n = 1$$

$$\frac{1}{2}\alpha_3^n + \alpha_4^n = 0.$$
(A.3)

This is satisfied by a one-parameter (call it β^n) family of solutions:

$$\alpha_1^n = 2 \quad \alpha_2^n = -2 - \frac{1}{2}\beta^n \quad \alpha_3^n = \beta^n \quad \alpha_4^n = -\frac{1}{2}\beta^n.$$
 (A.4)

For the second stage, $z^{n+1/2}$, z^n , $z^{n-1/2}$, z^{n-1} are available for the approximation. Similarly, letting

$$\Delta t \frac{dz}{dt}^{n+1/2,0} = \alpha_1^{n+1/2} z^{n+1/2} + \alpha_2^{n+1/2} z^n + \alpha_3^{n+1/2} z^{n-1/2} + \alpha_4^{n+1/2} z^{n-1}$$

$$= \Delta t \frac{dz}{dt} \Big|_{t_n} + \frac{1}{2} \Delta t^2 \frac{d^2 z}{dt^2} \Big|_{t_n} + \mathcal{O}\left(\Delta t^3\right)$$
(A.5)

and matching gives

$$\begin{split} \alpha_1^{n+1/2} + \alpha_2^{n+1/2} + \alpha_3^{n+1/2} + \alpha_4^{n+1/2} &= 0 \\ \frac{1}{2} \alpha_1^{n+1/2} - \frac{1}{2} \alpha_3^{n+1/2} - \alpha_4^{n+1/2} &= 1 \\ \frac{1}{2} \alpha_4^{n+1/2} &= \frac{1}{2} \,. \end{split} \tag{A.6}$$

This is also satisfied by a one-parameter $(\beta^{n+1/2})$ family of solutions:

$$\alpha_1^{n+1/2} = 4 + \beta^{n+1/2} \quad \alpha_2^{n+1/2} = -5 - 2\beta^{n+1/2} \quad \alpha_3^{n+1/2} = \beta^{n+1/2} \quad \alpha_4^{n+1/2} = 1 \,. \tag{A.7}$$

In practice, we take $\beta^n = 0$ to reduce the number of time levels involved and limit the number of potential parasitic modes introduced by the use of these backward difference approximations. This is reflected in the main text (see equation (21)).

B. Matrices used in linear stability analysis

The linear stability analysis of section 3.3.2 is derived in terms of two matrices A_1 and A_2 . These matrices are defined here.

matrices are defined here. Let
$$S = \sum_{j=0}^{k-1} \lambda_1^j \lambda_2$$
. Then

$$\mathbf{A}_{1} = \begin{bmatrix} 1 + \lambda_{1}^{k} + \frac{1}{2}\Delta tS & -\lambda_{1}^{k} & 0 & 0\\ 0 & 1 & 0 & 0\\ 0 & 0 & 1 & 0\\ 0 & 0 & 0 & 1 \end{bmatrix}$$
(B.1)

$$\mathbf{A}_{2} = \begin{bmatrix} 1 + \left(3 + \beta^{n+1/2}\right)\lambda_{1}^{k} + \Delta tS & -\left(6 + 2\beta^{n+1/2}\right)\lambda_{1}^{k} - \frac{1}{2}\Delta tS & \beta^{n+1/2}\lambda_{1}^{k} & \lambda_{1}^{k} \\ 0 & 1 & 0 & 0 \\ 0 & 0 & 1 & 0 \\ 0 & 0 & 0 & 1 \end{bmatrix}.$$
(B.2)

C. DNS algorithm

The motivating application for the development of the time discretization algorithm described in section 3 was the direct numerical simulation (DNS) of variable density turbulence. The spatial discretization used for this application and its interaction with the temporal discretization are described briefly here, as they were also used for the Rayleigh-Taylor test problem described in section 4.1.

The DNS algorithm described here is appropriate for simulation domains with periodic boundary conditions in two directions and was motivated by flows in unbounded domains where the timestep required for accuracy is similar to the timestep required for stability when using an explicit method [23]. The computational domain is $\mathcal{V} = [0, L_1] \times [-L_2/2, L_2/2] \times [0, L_3]$. A general flow variable f^1 is expressed as a Fourier series in x_1 and x_3 and expanded with B-splines in x_2 :

$$f(x_{1}, x_{2}, x_{3}, t) = \sum_{l=-\frac{N_{1}}{2}+1}^{\frac{N_{1}}{2}-1} \sum_{n=-\frac{N_{3}}{2}+1}^{\frac{N_{3}}{2}-1} \widehat{f}_{ln}(x_{2}, t) e^{ik_{1}x_{1}} e^{ik_{3}x_{3}}$$

$$= \sum_{l=-\frac{N_{1}}{2}+1}^{\frac{N_{1}}{2}-1} \sum_{j=0}^{N_{2}-1} \sum_{n=-\frac{N_{3}}{2}+1}^{\frac{N_{3}}{2}-1} f_{ljn}(t) e^{ik_{1}x_{1}} B_{j}(x_{2}) e^{ik_{3}x_{3}}$$

$$k_{1} = \frac{2\pi l}{L_{1}} \qquad k_{3} = \frac{2\pi n}{L_{3}}$$
(C.1)

Note that the dependence of k_1 and k_3 on l and n is assumed. A maximum continuity B-spline basis of order p [4, 5] is used for all solution variables except the x_2 component of momentum m_2 , which is represented with maximum continuity B-splines of order p+1. This enables mass conservation to be satisfied exactly as $\partial m_2/\partial x_2$ can be exactly represented in the function space used to represent other components of the state (see Appendix C.2). With this solution representation, a Fourier-Galerkin/B-spline-collocation method with approximate Galerkin quadrature is used to obtain the spatially discrete equations.

 $^{^1\}mathrm{We}$ drop the $\tilde{\cdot}$ notation previously used to distinguish spatially-discrete variables to simplify notation.

C.1. The divergence-free momentum

The 2-component of the curl and double curl of the momentum equations (8) are

$$\frac{\partial \Omega_2}{\partial t} = \frac{\partial^2}{\partial x_3 \partial x_j} \left(C_{1j} + \tau_{1j} \right) - \frac{\partial^2}{\partial x_1 \partial x_j} \left(C_{3j} + \tau_{3j} \right) \tag{C.2}$$

$$\frac{\partial \phi_2}{\partial t} = \frac{\partial^3}{\partial x_l \partial x_l \partial x_j} \left(C_{2j} + \tau_{2j} \right) - \frac{\partial^3}{\partial x_2 \partial x_l \partial x_j} \left(C_{lj} + \tau_{lj} \right) ,$$

$$\Omega_2 = \frac{\partial m_1^d}{\partial x_3} - \frac{\partial m_3^d}{\partial x_1} \qquad \phi_2 = \Delta m_2^d$$
(C.3)

with $C_{ij} \equiv -\rho u_i u_j$ and τ_{ij} is the viscous stress. Since equations (C.2) and (C.3) were obtained by applying the curl operators to the momentum equations, they leave \mathbf{m}^d averaged in x_1 and x_3 undetermined. Averaging the momentum equations over these directions and denoting such planar averages as $\overline{\cdot}^p$ gives:

$$\frac{\partial \overline{m}_{1}^{p}}{\partial t} = \frac{\partial}{\partial x_{2}} \left(\overline{C}_{12}^{p} + \overline{\tau}_{12}^{p} \right)
\frac{\partial \overline{m}_{3}^{p}}{\partial t} = \frac{\partial}{\partial x_{2}} \left(\overline{C}_{23}^{p} + \overline{\tau}_{23}^{p} \right)$$
(C.4)

where $\overline{m}_1^p = \overline{m^d}_1^p$, $\overline{m}_3^p = \overline{m^d}_3^p$, and $\overline{m^d}_2^p = 0$. The fact that $\partial \overline{\tau}_{ij}^p / \partial x_j$ simplifies to $\partial \overline{\tau}_{i2}^p / \partial x_2$ has also

Equations (C.2) to (C.4) govern the evolution of the divergence-free momentum. The main advantages of recasting the momentum equations in this way is that the pressure is eliminated and the divergencefree condition can be imposed exactly. For the modes with one or more non-zero wavenumbers, m_2^d is obtained in Fourier space from the Poisson problem

$$\widehat{\phi}_2 = -k^2 \widehat{m_2^d} + \frac{\partial^2 \widehat{m_2^d}}{\partial x_2^2} \tag{C.5}$$

where $k^2 = k_1^2 + k_3^2$ and we have suppressed the l and n indices for compactness. Then the x_1 and x_3 components are reconstructed by invoking the divergence-free condition and the definition of Ω_2 :

$$\widehat{m_1^d} = \frac{1}{k^2} \left(ik_1 \frac{\partial \widehat{m_2^d}}{\partial x_2} - ik_3 \widehat{\Omega}_2 \right)$$

$$\widehat{m_3^d} = \frac{1}{k^2} \left(ik_3 \frac{\partial \widehat{m_2^d}}{\partial x_2} + ik_1 \widehat{\Omega}_2 \right) .$$
(C.6)

Since the numerical representation of the x_2 dependence of $\widehat{m_1^d}$, $\widehat{m_3^d}$ and $\widehat{\Omega}_2$ can exactly represent the x_2 derivative of $\widehat{m_2^d}$, this procedure will produce m^d that is exactly divergence free.

C.2. The curl-free momentum and discrete conservation of mass

The mass conservation equation only involves the curl-free momentum in the x_2 direction (m_2^c) and in the direction of the wavevector $(k_1m_1^c + k_3m_3^c = \mathbf{k} \cdot \mathbf{m}^c)$. Mass conservation and the curl-free condition can thus be written in Fourier space as:

$$\frac{\widehat{df}}{dz}\frac{\widehat{\partial z}}{\partial t} = \frac{\partial \widehat{\rho}}{\partial t} = -ik\widehat{m}_{\parallel}^{c} - \frac{\partial \widehat{m}_{2}^{c}}{\partial x_{2}} \quad \text{mass conservation}$$

$$\frac{\partial \widehat{m}_{\parallel}^{c}}{\partial x_{2}} - ik\widehat{m}_{2}^{c} = 0 \quad \text{curl-free}$$
(C.7)

$$\frac{\partial \widehat{m}_{\parallel}^{c}}{\partial x_{2}} - ik\widehat{m}_{2}^{c} = 0$$
 curl-free (C.8)

where $m_{\parallel}^c \equiv \mathbf{k} \cdot \mathbf{m}/k$. A second curl-free constraint, $k_3 \widehat{m_1^c} - k_1 \widehat{m_3^c} = 0$, along with the definition of $\widehat{m_{\parallel}^c}$ allows $\widehat{m_1^c}$ and $\widehat{m_3^c}$ to be determined from $\widehat{m_{\parallel}^c}$ as

$$\widehat{m}_{1}^{c} = \frac{k_{1}}{k} \widehat{m}_{\parallel}^{c} \qquad \widehat{m}_{3}^{c} = \frac{k_{3}}{k} \widehat{m}_{\parallel}^{c}. \tag{C.9}$$

As $\partial \widehat{m_2^c}/\partial x_2$ is exactly represented in the function space used to represent $\widehat{m_\parallel^c}$, $\widehat{\rho}$, etc., if we require that (equation (C.7)) be satisfied without discretization error, mass conservation will be satisfied exactly. Therefore, we choose to enforce the boundary conditions on $\widehat{m_2^c}$ (see Appendix C.4) in lieu of satisfying equation (C.8) at the boundary when solving the coupled equations (C.7-C.8), which allows us to satisfy mass conservation at all collocation points. Hence, discretization error is isolated to equation (C.8) and mass conservation is achieved. Also, analogous to Appendix C.1, the planar averages of m^c must be determined as a special case, that is

$$\frac{\partial \overline{m^c}_2^p}{\partial x_2} = -\frac{\partial \overline{\rho}^p}{\partial t} \qquad \overline{m^c}_1^p = \overline{m^c}_3^p = 0.$$
 (C.10)

C.3. Time advance

This section details the time advance of the evolution equations with the temporal scheme established in section 3. The final DNS equations are

$$-\frac{df}{dz}\frac{\partial z}{\partial t} = \frac{\partial m_{j}^{c}}{\partial x_{j}}$$

$$\frac{\partial \Omega_{2}}{\partial t} = \frac{\partial^{2}}{\partial x_{3}\partial x_{j}}\left(C_{1j} + \tau_{1j}\right) - \frac{\partial^{2}}{\partial x_{1}\partial x_{j}}\left(C_{3j} + \tau_{3j}\right) = \mathcal{R}\mathcal{H}\mathcal{S}_{\Omega_{2}}$$

$$\frac{\partial \phi_{2}}{\partial t} = \frac{\partial^{3}}{\partial x_{l}\partial x_{l}\partial x_{j}}\left(C_{2j} + \tau_{2j}\right) - \frac{\partial^{3}}{\partial x_{2}\partial x_{l}\partial x_{j}}\left(C_{lj} + \tau_{lj}\right) = \mathcal{R}\mathcal{H}\mathcal{S}_{\phi_{2}}$$

$$\frac{\partial \overline{m}_{1}^{p}}{\partial t} = \frac{\partial}{\partial x_{2}}\left(\overline{C}_{12}^{p} + \overline{\tau}_{12}^{p}\right) = \mathcal{R}\mathcal{H}\mathcal{S}_{\overline{m}_{1}^{p}}$$

$$\frac{\partial \overline{m}_{3}^{p}}{\partial t} = \frac{\partial}{\partial x_{2}}\left(\overline{C}_{23}^{p} + \overline{\tau}_{23}^{p}\right) = \mathcal{R}\mathcal{H}\mathcal{S}_{\overline{m}_{3}^{p}}$$

$$\frac{\partial z}{\partial t} = \mathcal{L}(z)\frac{\partial z}{\partial t} + \mathcal{R}_{z}(z)$$

$$\rho = f(z).$$
(C.11)

The time advance of the state $S = (\phi_2, \Omega_2, z, \overline{m}_1^p, \overline{m}_3^p)$ over the course of one substep $s \to s + 1/2$ is outlined in Algorithm 2, which is an extension of Algorithm 1 to the spatially discrete problem defined by system (C.11). It is assumed

$$\mathcal{RHS}_{\Omega_{2}}^{s-1/2},\ \mathcal{RHS}_{\phi_{2}}^{s-1/2},\ \mathcal{RHS}_{\overline{m}_{1}^{p}}^{s-1/2},\ \mathcal{RHS}_{\overline{m}_{3}^{p}}^{s-1/2},\ \frac{\partial z}{\partial t}^{s-1/2,k_{f}}$$

are stored from the previous stage as well as the time history of z: $(z^s, z^{s-1/2}, z^{s-1}, z^{s-3/2})$ required for initializing the fixed-point problems.

Algorithm 2 Time advancement of system (C.11)

- 1: Finalize $m^{d,s}$ by solving equation (C.5) and applying equation (C.6).
- 2: Evaluate \mathcal{R}_z^s , generate BDF-like approximation of $\frac{\partial z}{\partial t}^{s,0}$.
- 3: Obtain $\frac{\partial z^{s,k_f}}{\partial t}$ as in section 3.2 then solve for m^c with equations (C.7) to (C.10).
- 4: Update thermodynamic and transport properties $(\rho^s, \mu^s, \mathcal{D}_z^s)$ which are known in terms of z^s .
- 5: Evaluate $\mathcal{RHS}_{\Omega_2}^s$, $\mathcal{RHS}_{\phi_2}^s$, $\mathcal{RHS}_{\overline{m}_1^p}^s$, $\mathcal{RHS}_{\overline{m}_1^p}^s$.
- 6: Time advance the state $S^s \to S^{s+1/2}$ with RK2. $z^s \to z^{s+1}$ uses $\frac{\partial z}{\partial t}^{s,k_f}$ and $\frac{\partial z}{\partial t}^{s-1/2,k_f}$, all other variables are advanced with the appropriate \mathcal{RHS}^s and $\mathcal{RHS}^{s-1/2}$.

C.4. Boundary conditions

Unbounded domains, often truncated for computational purposes, are commonly encountered in the simulation of turbulent flows, and that is the case in the x_2 direction here, in which the domain is formally infinite. In directions in which the turbulence is statistically homogeneous $(x_1 \text{ and } x_3)$, periodic boundary conditions are employed consistent with the use of Fourier expansions. In the x_2 direction, the momentum boundary condition is an extension of the potential-matching condition of Corral and Jiménez originally developed for incompressible flows [7]. This is based on the assumption that the vorticity decays rapidly as $x_2 \to \pm \infty$, so that at the boundary of a truncated computational domain the potential part of the velocity is consistent with a decaying irrotational solution in the exterior. In the variable-density case this means that, for L_2 sufficiently large, $\rho \to \rho_{\infty}$, $\nabla \times \boldsymbol{m} \to 0$, and $\nabla \cdot \boldsymbol{m} \to 0$.

Consider a potential-only momentum field for $x_2 > L_2/2$, so that $\mathbf{m} = \nabla \psi$. Then ψ obeys $\Delta \psi = 0$ and the Fourier coefficients of ψ satisfy $\hat{\psi} \sim e^{-kx_2}$, except when k = 0. Evaluating at the boundary of the computational domain $x_2 = L_2/2$, yields the potential-matching boundary conditions for the top boundary, and a similar analysis yields analogous conditions for the bottom boundary. They are:

$$\widehat{m}_{2}|_{\pm \frac{L_{2}}{2}} = \mp \frac{1}{k} \frac{\partial \widehat{m}_{2}}{\partial x_{2}} \Big|_{\pm \frac{L_{2}}{2}}$$

$$\widehat{m}_{1}|_{\pm \frac{L_{2}}{2}} = \mp \frac{ik_{1}}{k} \widehat{m}_{2}|_{\pm \frac{L_{2}}{2}}$$

$$\widehat{m}_{3}|_{\pm \frac{L_{2}}{2}} = \mp \frac{ik_{3}}{k} \widehat{m}_{2}|_{\pm \frac{L_{2}}{2}}$$
(C.12)

Clearly, both the divergence-free and curl-free components of m can satisfy these potential-matching condition individually, ensuring that m does as well.

Recall that $\Delta m_2^d = \phi_2$, so equation (C.3) is fourth order in m_2^d . Two additional boundary conditions on m_2^d are therefore needed. From the potential-matching condition, it follows that

$$k^{2} \widehat{m_{2}^{d}} \Big|_{\pm \frac{L_{2}}{2}} - \frac{\partial^{2} \widehat{m_{2}^{d}}}{\partial x_{2}^{2}} \Big|_{\pm \frac{L_{2}}{2}} = \widehat{\phi_{2}} \Big|_{\pm \frac{L_{2}}{2}} = 0, \tag{C.13}$$

A homogeneous Dirichlet boundary condition is thus applied to ϕ_2 . Then, when m_2^d is reconstructed from ϕ_2 via the Poisson equation equation (C.5), only the Robin conditions of equation (C.12) are explicitly enforced. A homogeneous Dirichlet condition is enforced on Ω_2 which is consistent with curlfree momentum at the boundary. When solving equations (C.7) and (C.8) for m_2^c and m_{\parallel}^c , the Robin conditions from equation (C.12) are imposed on $\widehat{m_2^c}$.

Averaging the mass conservation equation over x_1 and x_3 yields a homogeneous Neumann condition on \overline{m}_2^p at the boundary, since the flow is essentially constant density there. This means there is one remaining degree of freedom when determining \overline{m}_2^p which is used to enforce a symmetry condition or set the value at a location in the domain, for example. For the Rayleigh-Taylor problem, simulations are stopped well before the front nears the boundary so a homogeneous Dirichlet condition is used at the top of the domain as the fluid remains at rest.

Homogeneous Neumann conditions are imposed on the streamwise and spanwise plane-averaged momentum as well as the plane-averaged and fluctuating components of the transported scalar, z.

D. Convergence and simulation specifics for Rayleigh-Taylor problem

To determine the spatial resolution used for the single-mode Rayleigh-Taylor cases detailed in section 4, the 2D problem with At = 0.5 and Re = 3000 was simulated with three different meshes: $N_1 \times N_2 = 64 \times 256$, 128×512 , and 256×1024 . Note that the Atwood number is low enough to use the smaller computational domain in the vertical direction ($x_2 \in [2W, 2W]$). The timestep details are given in table D.1. Comparisons of the bubble and spike locations over time (figure D.8) as well as contours of the interface for later times (figure D.9, z = 0.5) show no discernible differences in the solutions with changing resolution. The maximum variation of the bubble height h_b/W amongst the different resolutions, for example, is ~ 0.002 at $t\sqrt{At}/\sqrt{W/g} = 3$ when the height itself is ~ 0.8 . A Richardson extrapolation procedure using the three solutions suggests an absolute error of $\mathcal{O}(10^{-4})$, corresponding to relative errors of $\mathcal{O}(10^{-2})\%$, in the bubble height for late times on the second grid. As simulations for

higher Atwood numbers were desired, the resolution suggested by the second grid was selected for the cases shown in this work. Subsequently, a similar Richardson extrapolation of the time discretization was performed with three different timesteps: $\Delta t \sqrt{A}t/\sqrt{W/g} = 2.5 \times 10^{-4}$, 1.25×10^{-4} , and 6.25×10^{-5} . This indicated the scheme is second order as expected and that for the timestep specified in table D.1 $(\Delta t \sqrt{A}t/\sqrt{W/g} = 2.5 \times 10^{-4})$ the late time errors in bubble height are $\mathcal{O}(10^{-7})$, corresponding to relative errors of $\mathcal{O}(10^{-5})\%$.

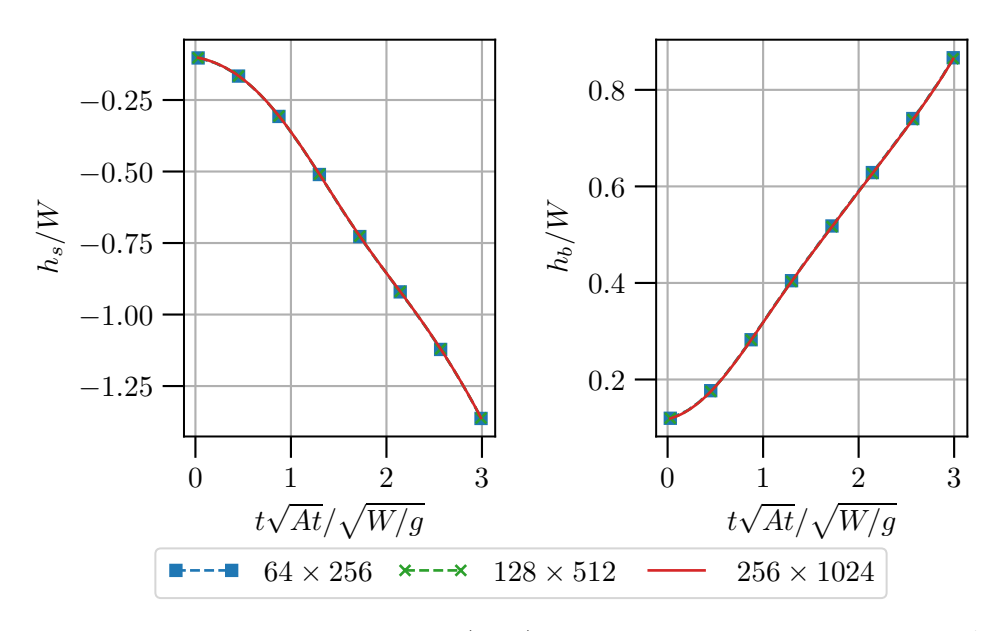


Figure D.8: Evolution of the bubble and spike height (h_b, h_s) in the Rayleigh-Taylor test problem with At = 0.5 in two dimensions using three different resolutions.

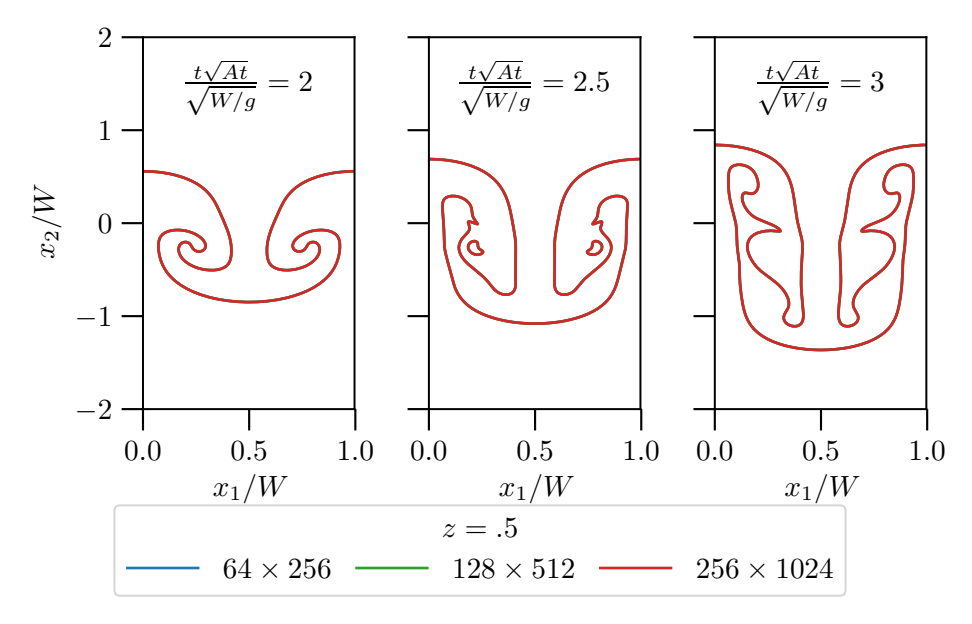


Figure D.9: Location and shape of the fluid interface (the z=.5 contour) in the Rayleigh-Taylor test problem in two dimensions with At=0.5 at late times. Results for three different resolutions are shown.

For the cases presented in the text and this appendix, the computational domain, grid spacing, and timestep employed are listed in table D.1. The domains are defined as follows:

$$\mathcal{V}_{RT}^{2D,1} = \left[0,W\right] \times \left[-2W,2W\right], \qquad \qquad 128 \times 512 \, \mathrm{mesh}; \label{eq:VRT}$$

Table D.1: Domain and timestep specification for Rayleigh-Taylor cases presented in section 4.

At	Dimension	Re	Domain	$\Delta t \sqrt{At}/\sqrt{W/g}$
.33	2	3000	$\mathcal{V}_{RT}^{2D,1}$	2.5×10^{-4}
.5	2	3000	$\mathcal{V}_{RT}^{2D,1}$	2.5×10^{-4}
.67	2	3000	$\mathcal{V}_{RT}^{2D,1}$	2.5×10^{-4}
.8	2	3000	$\mathcal{V}_{RT}^{2D,1}$	2.5×10^{-4}
.925	2	3000	$\mathcal{V}_{RT}^{2D,2}$	1.25×10^{-4}

At	Dimension	Re	Domain	$\Delta t \sqrt{At}/\sqrt{W/g}$
.33	3	1024	$\mathcal{V}_{RT}^{3D,1}$	2.5×10^{-4}
.5	3	1024	$\mathcal{V}_{RT}^{3D,1}$	2.5×10^{-4}
.67	3	1024	$\mathcal{V}_{RT}^{3D,2}$	1.25×10^{-4}
.8	3	1024	$\mathcal{V}_{RT}^{3D,2}$	6.25×10^{-5}
.925	3	1024	$\mathcal{V}_{RT}^{2D,2}$	3.125×10^{-5}

$$\begin{split} \mathcal{V}_{RT}^{2D,2} &= [0,W] \times [-3.5W, 3.5W] \,, \\ \mathcal{V}_{RT}^{3D,1} &= [0,W] \times [-2W, 2W] \times [0,W] \,, \\ \mathcal{V}_{RT}^{3D,2} &= [0,W] \times [-3.5W, 3.5W] \times [0,W] \,, \end{split} \qquad \begin{aligned} &128 \times 1024 \, \text{mesh}; \\ &128 \times 512 \times 128 \, \text{mesh}; \\ &128 \times 1024 \times 128 \, \text{mesh}. \end{aligned}$$

References

- [1] Almagro, A., García-Villalba, M., Flores, O., 2017. A numerical study of a variable-density low-speed turbulent mixing layer. Journal of Fluid Mechanics 830, 569–601.
- [2] Bell, J., 2005. AMR for low Mach number reacting flow, in: Adaptive Mesh Refinement-Theory and Applications. Springer, pp. 203–221.
- [3] Bertaccini, D., Durastante, F., 2018. Iterative methods and preconditioning for large and sparse linear systems with applications. CRC Press.
- [4] de Boor, C., 2001. A practical guide to splines revised edition. Springer-Verlag, New York .
- [5] Botella, O., Shariff, K., 2003. B-spline methods in fluid dynamics. International Journal of Computational Fluid Dynamics 17, 133–149.
- [6] Brown, D.L., Cortez, R., Minion, M.L., 2001. Accurate projection methods for the incompressible navier-stokes equations. Journal of computational physics 168, 464-499.
- [7] Corral, R., Jiménez, J., 1995. Fourier/chebyshev methods for the incompressible navier-stokes equations in infinite domains. Journal of Computational Physics 121, 261–270.
- [8] Ding, H., Spelt, P.D., Shu, C., 2007. Diffuse interface model for incompressible two-phase flows with large density ratios. Journal of Computational Physics 226, 2078–2095.
- [9] Dodd, M.S., Ferrante, A., 2014. A fast pressure-correction method for incompressible two-fluid flows. Journal of Computational Physics 273, 416–434.
- [10] Domino, S.P., Hewson, J., Knaus, R., Hansen, M., 2021. Predicting large-scale pool fire dynamics using an unsteady flamelet- and large-eddy simulation-based model suite. Physics of Fluids 33, 085109.
- [11] Goncharov, V.N., 2002. Analytical model of nonlinear, single-mode, classical Rayleigh-Taylor instability at arbitrary Atwood numbers. Physical Review Letters 88, 4.
- [12] Greenbaum, A., 1997. Iterative methods for solving linear systems. SIAM.
- [13] Guermond, J., Minev, P., Shen, J., 2006. An overview of projection methods for incompressible flows. Computer Methods in Applied Mechanics and Engineering 195, 6011–6045.
- [14] Hamzehloo, A., Bartholomew, P., Laizet, S., 2021. Direct numerical simulations of incompressible Rayleigh-Taylor instabilities at low and medium Atwood numbers. Physics of Fluids 33, 054114.
- [15] He, X., Zhang, R., Chen, S., Doolen, G.D., 1999. On the three-dimensional Rayleigh-Taylor instability. Physics of Fluids 11, 1143–1152.
- [16] Jang, Y., de Bruyn Kops, S.M., 2007. Pseudo-spectral numerical simulation of miscible fluids with a high density ratio. Computers and Fluids 36, 238–247.
- [17] Kim, J., Moin, P., Moser, R., 1987. Turbulence statistics in fully developed channel flow at low Reynolds number. Journal of fluid mechanics 177, 133–166.
- [18] Knikker, R., 2011. A comparative study of high-order variable-property segregated algorithms for unsteady low Mach number flows. International Journal for Numerical Methods in Fluids 66, 403–427.
- [19] Lee, H.G., Kim, J., 2013. Numerical simulation of the three-dimensional Rayleigh-Taylor instability. Computers & Mathematics with Applications 66, 1466–1474.
- [20] Lu, X., Pantano, C., 2020. On mass conservation and solvability of the discretized variable-density zero-mach navierstokes equations. Journal of Computational Physics 404, 109132.
- [21] Malaya, N., Estacio-Hiroms, K.C., Stogner, R.H., Schulz, K.W., Bauman, P.T., Carey, G.F., 2013. MASA: a library for verification using manufactured and analytical solutions. Engineering with Computers 29, 487–496.
- [22] Mallik, R.K., 1998. Solutions of linear difference equations with variable coefficients. Journal of Mathematical Analysis and Applications 222, 79–91.
- [23] Moin, P., Mahesh, K., 1998. Direct numerical simulation: a tool in turbulence research. Annual review of fluid mechanics 30, 539–578.
- [24] Moser, R.D., 2023. Numerical challenges in turbulence simulation, in: Numerical Methods in Turbulence Simulation. Elsevier, pp. 1–43.
- [25] Motheau, E., Abraham, J., 2016. A high-order numerical algorithm for DNS of low-Mach-number reactive flows with detailed chemistry and quasi-spectral accuracy. Journal of Computational Physics 313, 430–454.
- [26] Najm, H.N., Wyckoff, P.S., Knio, O.M., 1998. A semi-implicit numerical scheme for reacting flow: I. Stiff chemistry. Journal of Computational Physics 143, 381–402.
- [27] Nicoud, F., 2000. Conservative high-order finite-difference schemes for low-Mach number flows. Journal of Computational Physics 158, 71–97.
- [28] Pierce, C.D., 2001. Progress-Variable Approach For Large-Eddy Simulation Of Turbulent Combustion. Ph.D. thesis. Stanford University.
- [29] Rauwoens, P., Vierendeels, J., Merci, B., 2009. A stable pressure-correction scheme for time-accurate non-premixed combustion simulations. Flow, Turbulence and Combustion 82, 249–269.
- [30] Reuter, B.W., 2021. A reacting jet direct numerical simulation for assessing combustion model error. Ph.D. thesis. The University of Texas-Austin.
- $[31]\,$ Saad, Y., 2003. Iterative methods for sparse linear systems. SIAM.
- [32] Shunn, L., Ham, F., 2006. Consistent and accurate state evaluations in variable-density flow simulations. Annual Research Briefs, 135–147.
- [33] Tomboulides, A., Lee, J., Orszag, S., 1997. Numerical simulation of low mach number reactive flows. Journal of Scientific Computing 12, 139–167.
- [34] Wall, C., Pierce, C.D., Moin, P., 2002. A semi-implicit method for resolution of acoustic waves in low Mach number flows. Journal of Computational Physics 181, 545–563.